Ultrafast Science
A SCIENCE PARTNER JOURNAL

RESEARCH ARTICLE

Complete Electric Field Characterization of Ultrashort Multicolor Pulses

Maximilian Kubullek[1,2], Miguel A. Silva-Toledo[1,2], Roland E. Mainz[1,2], Fabian Scheiba[1,2], Rafael de Q. Garcia[1,2], Felix Ritzkowsky[1,2], Giulio Maria Rossi[1,2*], and Franz X. Kärtner[1,2]

[1]Center for Free-Electron Laser Science CFEL, Deutsches Elektronen-Synchrotron DESY, 22607 Hamburg, Germany. [2]Physics Department and The Hamburg Centre for Ultrafast Imaging (CUI), University of Hamburg, 22607 Hamburg, Germany.

*Address correspondence to: giulio.maria.rossi@desy.de

Citation: Kubullek M, Silva-Toledo MA, Mainz RE, Scheiba F, de Q. Garcia R, Ritzkowsky F, Rossi GM, Kärtner FX. Complete Electric Field Characterization of Ultrashort Multicolor Pulses. *Ultrafast Sci.* 2025;5:Article 0081. https://doi.org/10.34133/ultrafastscience.0081

Submitted 12 November 2024
Revised 17 January 2025
Accepted 20 January 2025
Published 12 February 2025

The advancement of laser technology, producing increasingly shorter and more intricate optical pulses, has elevated the significance of precise characterization of a transient electric field, including the carrier-envelope phase. This characterization must cover progressively larger spectral bands and be performed as close as possible to the experimental site to enable a detailed understanding of the coherent light–matter interaction. Furthermore, in many experiments, two (or more) different ultrashort pulses are used, calling for a technique capable of characterizing multiple electric fields simultaneously. Here, we introduce the TREX (third-order reconstruction of electric fields via cross(X)-correlation) method, which allows the all-optical, in situ characterization of the complete electric fields of 2 broadband pulses with different central wavelengths. The method relies on the measurement of the perturbative third-order nonlinear response generated in a noble gas target while varying the delay between 2 pulses. The resulting spectrograms can be reconstructed using a custom evolutionary algorithm. The technique is demonstrated by retrieving the complete electric field, including the carrier-envelope phase, generated by the coherent synthesis of 2 ultrashort pulses. These synthesized waveforms reach time durations below a single optical cycle, demonstrating the ability of TREX to characterize complex multioctave-spanning electric fields.

Introduction

Advances in ultrafast physics experiments have largely been enabled by the implementation of numerous pulse characterization techniques suitable for different experimental conditions. The most widely used all-optical techniques are based on the measurement of parameterized nonlinear process spectra and iterative reconstruction [1], the most prominent of which are frequency-resolved optical gating (FROG) [2,3] and dispersion scan (d-scan) [4,5]. Alternatively, spectral phase interferometry techniques, such as spectral phase interferometry for direct electric-field reconstruction [6,7] and 2-dimensional spectral shearing interferometry [8,9], allow directly accessing the group delay.

These characterization techniques return the spectrum and spectral phase but typically do not allow access to the carrier-envelope phase (CEP), an extremely important parameter in pulses with few optical cycles. However, when the pulse presents an octave-spanning spectrum, interference between the fundamental and the second harmonic can be observed and used to reconstruct the CEP, as demonstrated using the d-scan technique [10]. Yet, this opportunity is limited to spectral regions where the phase matching of nonlinear crystals—essential for obtaining the second-order signal—is such that conversion of octave-spanning spectra is possible. Since the CEP is often a crucial parameter, it is typically determined using a separate setup based on either spectral interference [11] or above-threshold ionization [12]. The separation of spectral phase and CEP measurement has the disadvantage that the actual optical waveform at the point of interest can be inferred only by numerical propagation of the results obtained from the distinct measurements and, thus, with high uncertainty.

Several field sampling techniques have been developed in recent years to tackle this problem [13]. These methods are based either on highly nonlinear processes, such as ionization [14–19], carrier injection [20–23], and high-harmonic generation [18], or on perturbative nonlinearities, such as electro-optic sampling [24]. Although these methods resolve the ambiguity related to the CEP by returning the electric field in the time domain, they require sophisticated modeling of the nonlinear interaction, susceptible to quantitative errors, and/or a complex experimental apparatus, and/or a shorter sampling pulse, which is not always available.

A common limitation is that the pulse characterization often takes place under conditions different from those used in the experiment, e.g., at a different position or using a pulse replica. An important step to circumvent this limitation was taken by Crespo et al. [25], who demonstrated in situ pulse characterization simultaneous to the generation of high harmonics by performing a third-harmonic d-scan (THIS:d-scan). In their case,

access to the CEP and, thus, to the complete optical waveform was not possible, although the authors suggest that it would have been possible for pulses with a bandwidth greater than one octave. Another recent publication by Awad et al. [26] demonstrated a method combining the principle of TIPTOE (tunneling ionization with a perturbation for the time-domain observation of an electric field) with high-harmonic generation from solids to perform in situ pulse characterization.

The scenario in which 2 (or more) spectrally different pulses interact with a sample is common in ultrafast science, such as in nondegenerate pump–probe spectroscopy [27] or in the wide variety of $\omega - 2\omega$ [28,29] and $\omega - 3\omega$ experiments [30,31]. In these experiments, a precise characterization of the relative delay between the pulses is also crucial. Multiple techniques capable of characterizing 2 pulses of different colors have been demonstrated including very advanced method for phase and intensity retrieval of e-fields [32] and double-blind FROG [33]. So far, none of these techniques have allowed the complete reconstruction of 2 spectrally different electric fields, including both CEPs.

In this article, we introduce a technique called TREX, which stands for third-order reconstruction of electric fields via cross(X)-correlation. It allows the in situ reconstruction of 2 spectrally different pulses, as well as their relative delay, without needing any additional reference pulse. Importantly, if the pulses are ultrabroadband, their CEPs can also be determined, allowing for a complete field reconstruction.

TREX is implemented by focusing 2 collinearly propagating pulses into a gas target (see the top of Fig. 1). The spectrum generated by the gas nonlinearity (predominantly third order [TO]) is recorded while varying the delay between the pulses, generating a spectrogram as depicted in Fig. 1C. The collinear geometry gives rise to interference fringes that are sensitive to the phase difference between the pulses (including the relative phase φ_r), similarly to interferometric FROG [34] (see the φ_r arrows in Fig. 1C). When dealing with CEP-stable few-cycle pulses ($\mathrm{CEP}_1 = \varphi_0$ and $\mathrm{CEP}_2 = \varphi_0 + \varphi_r$), additional fringes appear in the spectrogram (indicated in Fig. 1C by the φ_0 arrow) that are sensitive to the common phase φ_0 of the pulses, allowing the TREX reconstruction algorithm to determine the full electric fields of both pulses including their CEPs.

We demonstrate the TREX technique by characterizing 2 CEP-stable few-cycle pulses generated by a multistage optical parametric amplifier (OPA) system [35]. The spectra of the 2 pulses span 700 to 1,000 nm (near-infrared [NIR] pulse) and 1,200 to 2,200 nm (infrared [IR] pulse). These pulses can be coherently combined to produce synthesized waveforms with an intensity full width at half maximum duration down to 2.8 fs, corresponding to a half-cycle pulse. Due to the extreme sensitivity of the synthesized waveforms on the relative delay, the CEPs, and the precise envelope shapes of the 2 constituent pulses, our synthesizer is an ideal test case for the TREX technique. Knowledge of the electric field waveform is crucial for strong-field interactions, such as high-harmonic generation, which is an important application of our synthesized pulses.

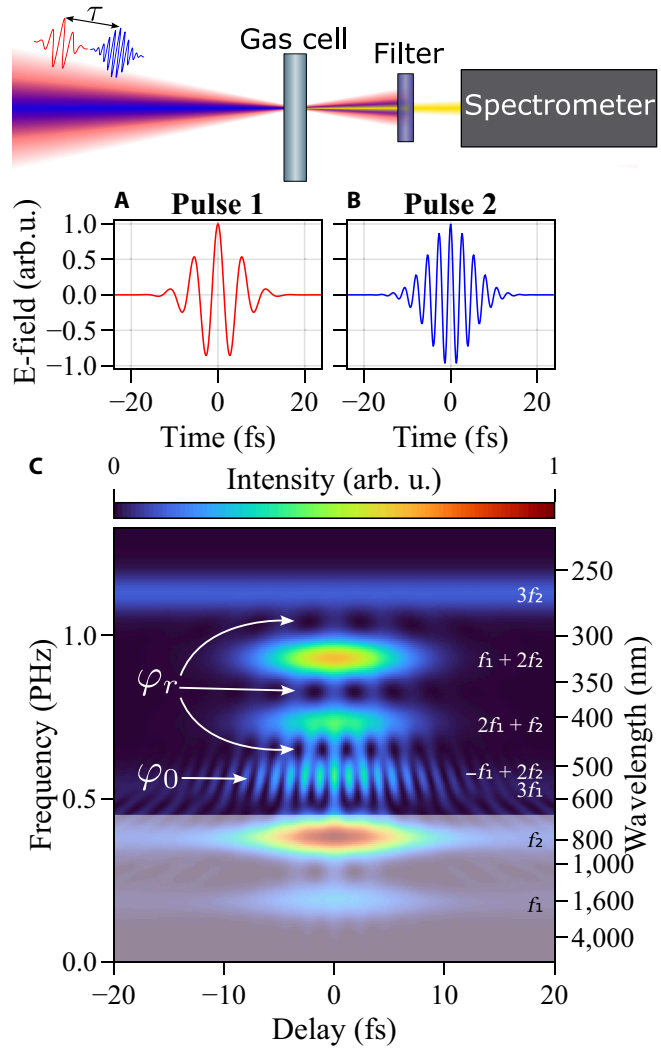

Fig. 1. Top: Experimental geometry of the TREX (third-order reconstruction of electric fields via cross(X)-correlation) method. Two collinearly propagating pulses are focused into a gas target and the spectrum of the third-order (TO) nonlinear signal is recorded for varying delay τ. Bottom: Simulated TO spectrogram (C) for 2 Fourier-limited Gaussian pulses with central wavelengths of (A) 1,700 nm ($f_1 \approx 0.18$ PHz) and (B) 800 nm ($f_2 \approx 0.37$ PHz). The TO-mixing terms are indicated at the right side of (C). The arrows indicate φ_r- and φ_0-sensitive regions. Note that this simulation shows only the nonlinear part of the signal. The shaded region is experimentally not observed due to the copropagating fundamentals and is not shown in the next figures. E-field, electric field.

Methods

Simple model

The TO nonlinear polarization of a gas medium generates new frequencies over multiple spectral regions via different 4-wave-mixing channels, shown in Fig. 1C. For the experimental TREX measurements presented in this paper, we detect the TO signal over the ultraviolet (UV)-to-NIR range (enabled by silicon-based detectors). When considering a helium gas target with a pressure of 1 bar, the wave vector mismatch with the fundamental is at most in the 10^{-8}-nm^{-1} range, corresponding to a coherence length of several centimeters (see supplementary document Section S1). Since the medium length of about 1 mm is much shorter than the coherence length, we neglect phase matching in our simple theoretical description. The frequency dependence of the nonlinear susceptibility is neglected since a noble gas medium with a high ionization potential is used. Additionally, if we assume an ionization fraction of the gas of <0.1%, the plasma-induced reshaping of the fundamental pulses can be neglected. Under these assumptions, the TO

polarization, including all mixing signals, can be calculated in the time domain using the following equation:

$$P_{NL}(t,\tau) \propto \left[E_1(t-\tau)+E_2(t)\right]^3, \quad (1)$$

whereby $E_1(t)$ and $E_2(t)$ are the real-valued electric fields of the 2 pulses and τ is the delay between them. We will later refer to the sum of the individual electric fields as the total field:

$$E_{tot}(t,\tau) = E_1(t-\tau) + E_2(t). \quad (2)$$

The individual fields are described by

$$E_1(t) = A_1(t)\cos\left(2\pi f_1 t + \varphi_0 + \mathcal{O}\left(t^2\right)\right) \quad (3)$$

$$E_2(t) = A_2(t)\cos\left(2\pi f_2 t + \varphi_0 + \varphi_r + \mathcal{O}\left(t^2\right)\right) \quad (4)$$

where $\mathcal{O}\left(t^2\right)$ include all higher-order dispersions of each pulse. It is important to note that in this description, a variation of the common phase φ_0 leads to an equal variation of the CEP of E_{tot}.

To describe the actual measured frequency domain signal $\tilde{S}(f,\tau)$ we take into account the transfer function $T(f)$ of the optical setup. The measured signal is then given by

$$\tilde{S}(f,\tau) \propto \left| f \;\; \mathcal{FT}\left\{P_{NL}(t,\tau)\right\}\right|^2 \cdot T(f). \quad (5)$$

In the frequency domain, the signal $\tilde{S}$ contains contributions from all 4-wave-mixing terms of the 2 spectra.

To verify the validity of this simple model under realistic conditions, we performed 2-dimensional (radial symmetry) nonlinear propagation simulations using the Luna.jl package [36] and compared the corresponding spectrograms (see supplementary document Section S2).

Figure 1C shows a TO spectrogram calculated using Eq. 5 for 2 Gaussian pulses with central wavelengths of 1,700 and 800 nm, respectively (Fig. 1A and B), which are close to those of the pulses characterized in the experiments. The horizontal lines in this plot correspond to the delay-independent contributions, which are the third-harmonic ($3f_1$ and $3f_2$) and self-phase modulation (SPM) ($f_1+f_1-f_1$ and $f_2+f_2-f_2$) of the 2 pulses. During the temporal overlap, the delay-dependent terms appear. These are the cross-phase modulation (XPM) terms ($f_1+f_2-f_2$ and $f_2+f_1-f_1$) and the mixing terms $2f_2-f_1$, $2f_1+f_2$, and f_1+2f_2. In principle, additional mixing terms can appear at lower frequencies than the fundamentals. For the 2 central frequencies analyzed here, these mixing terms fall into the mid- to far-IR region and are thus experimentally not observable in our setup. Nevertheless, they can be easily observed for pulses in the UV and visible range.

Chirp sensitivity

As for FROG or d-scan, the mixing signals encode the spectral phase of the 2 pulses. Figure 2 illustrates the effects of second- (group delay dispersion [GDD]) and third-order dispersion (TOD) on the spectrogram. GDD leads to a tilting of the mixing signals due to the change in the instantaneous frequency of the pulses. TOD, on the other hand, leads to an asymmetric deformation of the signals stemming from the typical pre- or post-pulses generated by TOD. It is important to note that chirping 1 of the 2 pulses does not simply produce the opposite behavior of chirping the other one. As shown in Fig. 2A and C, the spectrograms resulting from chirping one pulse or the other are qualitatively different. This allows the TREX technique to unambiguously determine the chirp of each pulse.

To demonstrate that the chirp can be accurately reconstructed from the spectrograms, we performed 2 measurements, before and after inserting a fused silica window into the beam path of both pulses. The material phase was determined by subtracting the reconstructed spectral phases of the 2 measurements, as shown in Fig. 3 alongside the expected phase shift calculated from the Sellmeier equation [37]. The

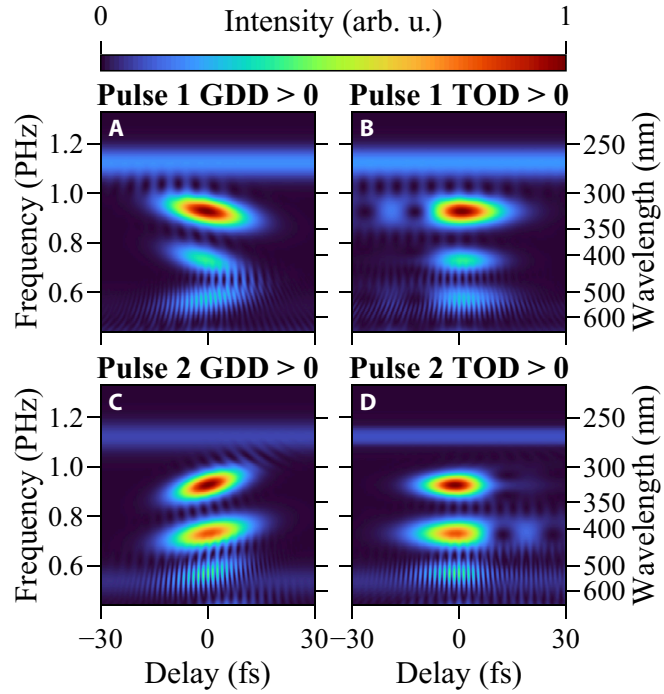

Fig. 2. Simulated spectrograms for the same pulses as in Fig. 1C, when group delay dispersion (GDD) (A and C) or third-order dispersion (TOD) (B and D) are applied to 1 of the 2 pulses, showing the typical tilting or asymmetric broadening.

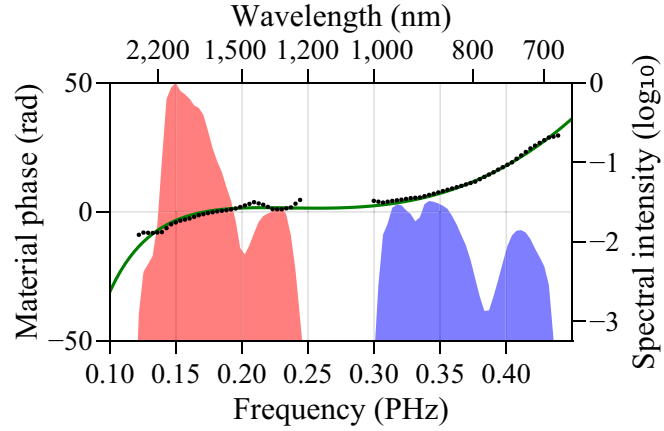

Fig. 3. Green line: Expected phase shift due to propagation through 1.9 mm of fused silica. Black dots: Phase shift obtained by subtracting the spectral phases reconstructed through 2 consecutive TREX measurements, made before and after adding (2.0 ± 0.1) mm of fused silica in the beam path of both pulses.

phase shift agrees well with the expected one. We attribute the slight deviation of the phase around 1,400 nm to the small O–H absorption line of the UV-fused silica substrate used for the measurement. The measured and retrieved spectrograms underlying the shown result can be found in supplementary document Section S12.

Common- and relative-phase sensitivity

When the 2 pulses have broad spectra and different central frequencies, the various mixing terms spectrally overlap. This leads to beatings along the delay axis, which are sensitive to the relative phase φ_r between the 2 pulses. Furthermore, the fringes arising from the interference of [SPM/XPM and $3f_1$], [$2f_2 - f_1$ and $3f_1$], and [$2f_2 - f_1$ and $2f_1 + f_2$] show also a dependence on the common phase φ_0. In the absence of φ_0 stability, these fringes will disappear when averaged over multiple shots, even if φ_r is stable. However, other fringes, such as those arising from the interference between $f_1 + 2f_2$ and $2f_1 + f_2$, will still be visible even if only φ_r is stable. In this case, one can still determine the spectral phase of both pulses and the intensity envelope of the total field, which is generated by summing the 2 pulses coherently. In the absence of relative-phase stability, all fringes will be washed out, and only the individual envelopes and chirps, but not the envelope and chirp of the total field, can be determined (see supplementary document Sections S3 and S4).

In the presence of phase stability, the fringes allow the reconstruction of the total field, including the CEP, up to an unknown global sign of the total electric field, since these phase-dependent fringes are referenced to the envelope-dependent signals (as they both appear on the same spectrogram). This remaining ambiguity stems from the inherent inversion symmetry of the atomic system and manifests itself in a π periodicity of the φ_0-dependent fringes when scanning φ_0. The dynamics of the fringes during a φ_0 and a φ_r scan are presented in Movies S1 and S2.

One should note that for different bandwidths and ratios between the central frequencies of the 2 pulses, the φ_0-dependent fringes might arise from a different combination of interfering mixing terms or might not be present at all for narrowband pulses. The dependency of the 4-wave mixing signals on the f_1/f_2 ratio is shown in supplementary document Section S6, both in the case of 2 "long" (8-cycle) pulses and in the case of 2 "short" (2-cycle) pulses. Fringes depending on φ_0 (and on φ_r) are expected at each crossing point. For 2-cycle and shorter pulses, φ_0-dependent fringes appear for practically any ratio f_2/f_1, given the broad bandwidth. In general, φ_0 -dependent fringes arise from the interference of two 4-wave mixing signals that exhibit a different dependence on φ_0. For example, shifting φ_0 by $\Delta\varphi_0$ leads to a phase shift of $3\Delta\varphi_0$ for the $3f_1$ signal, while the phase of the $-f_1 + 2f_2$ term changes by $\Delta\varphi_0$, giving φ_0 sensitivity to the interference signal among the 2 terms, which occurs for $f_2/f_1 \approx 2$.

Figure 4A shows the evolution of the measured spectrum for a fixed delay, close to time zero, while linearly scanning φ_0. This experiment was performed by utilizing the control system of the waveform synthesizer that allows the independent control of φ_0 and φ_r [38]. In particular, the $f-2f$ signal measured in the multiphase meter of the control system returns the phase $\varphi_{pm} = \varphi_0 + \text{const}$. Initially, the constant is not known. The data presented in Fig. 4A were acquired while locking φ_r to a fixed value and linearly scanning φ_{pm} over a 3π range multiple times. The in-loop $f-2f$ data of the control system as well as all

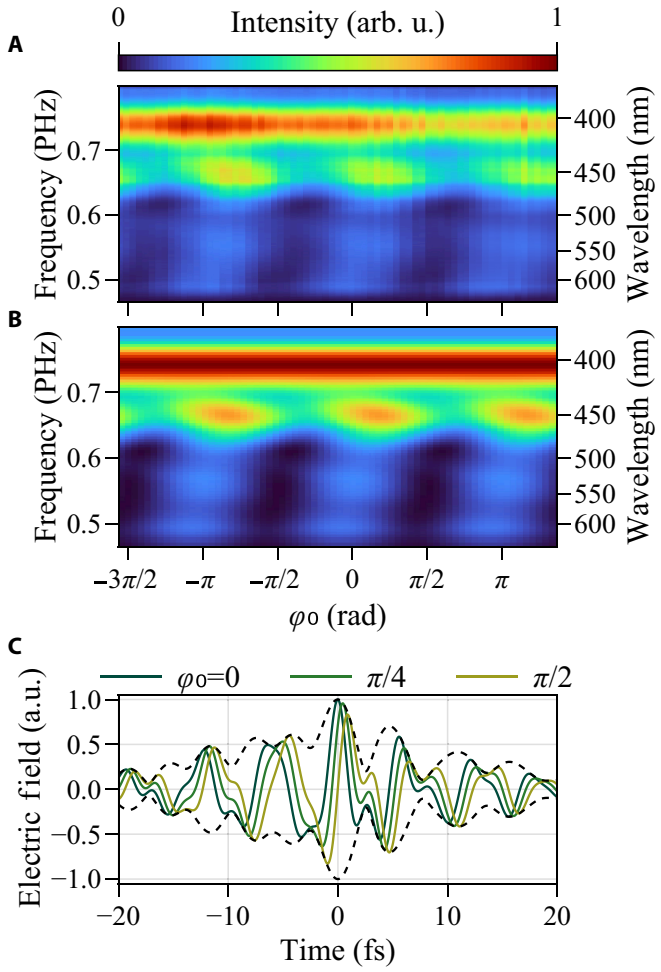

Fig. 4. Carrier-envelope phase (CEP) (φ_0) dependence of the TREX signal. (A) Measured TREX spectrogram while varying φ_0 at a fixed delay and φ_r. The expected π periodicity is visible. (B) Simulated φ_0 scan using the pulses characterized before acquiring the data in (A). (C) E_{tot} for 3 different positions in the φ_0 scan. The dashed line indicates the electric field envelope.

acquired TO spectra are shown in supplementary document Section S5. The measured single-shot φ_{pm} values allow us to assign a phase axis to the measured spectra. In order to determine the unknown constant ($\varphi_{pm} - \varphi_0$), we performed a TREX measurement directly before the φ_0 scan, at a known fixed φ_{pm} value. The electric fields retrieved from this TREX measurement provide an absolute value of φ_0 and therefore allow us to determine the constant offset between φ_0 and φ_{pm}. This enables the unambiguous determination of the complete E_{tot} for each acquired spectrum and corresponding φ_0 value. In particular the fringe maximum ($\varphi_0 = 0 \pm n\pi$) corresponds to the field shape E_{tot} that maximizes the instantaneous intensity (dark green line in Fig. 4C).

The experimental data are compared to a simulation (see Fig. 4B), based on the simple model presented earlier, obtained by numerically varying the φ_0 of E_{tot} retrieved from the TREX measurement. The very good agreement, which extends to the substructure of the beatings, showcases the accuracy of the retrieved optical waveforms. Please note that the scale of the φ_0 axis is provided by the single-shot φ_{pm} data, measured independently by the $f-2f$ phase meter, and was not further adjusted to fit the expected π periodicity. This measurement

shows that TREX is sensitive also to the common phase φ_0 and can thus reconstruct the complete electric fields of both pulses, including their CEPs ($CEP_1 = \varphi_0$; $CEP_2 = \varphi_0 + \varphi_r$).

It is worth noting that for the experimentally used condition (frequency ratio ≈ 2.1), the interference of the XPM/SPM signal of f_2 and the third harmonic of f_1 generates a beating signal that oscillates along the delay axis with a period corresponding exactly to the optical frequency at which it is observed. This allows a precise calibration of the delay axis, thus a self-referenced measurement, provided that the frequency axis of the spectrometer is calibrated (for more details, see supplementary document Section S7).

It is also important to observe that the TREX TO signal is generated in a region around the focus that extends only across a fraction of the Rayleigh length, given its proportionality to $\left(E_{tot}\right)^3$. This ensures that the Gouy phase assumes a well-defined mean value during the TO-signal generation. Nevertheless, in order to achieve CEP sensitivity, it is important that the nonlinear medium provides a sufficiently low dispersion such that the waveforms do not change drastically during propagation.

High-intensity effects

A key requirement for the simple model to be valid is that the peak intensity of E_{tot} does not exceed about 0.5 PW cm^{-2} for a nonlinear interaction length of ~1 mm, in helium with a backing pressure of about 1 bar, if few-cycle pulses are assumed. For higher intensities (or longer interaction lengths), the generated TO signal can itself undergo another TO interaction with the copropagating fundamentals. The resulting radiation generated through this cascaded effect reaches the fifth harmonic spectral region (and beyond) and, importantly, overlaps spectrally with the initial TO signal, forming additional fringes, which distort the spectrogram around time zero, where the peak intensity is the highest.

Furthermore, a high peak intensity can lead to substantial ionization [39]. The resulting plasma not only creates additional signals (such as blueshift [40] or Brunel harmonics [41]), not taken into account by our simple model, but can also dramatically change the total field as it propagates through the gas target, preventing an accurate reconstruction of the 2 electric fields. Due to the highly nonlinear process, ionization-induced distortions are stronger close to time zero, where the peak field increases dramatically if the 2 constituent pulses are phase stable and, therefore, coherently combined.

Since the retrieval algorithm introduced in the following section relies on the simple model to be computationally efficient, care has to be taken to avoid ionization and cascaded effects. This can be easily achieved either by keeping the pulse intensities low enough or by decreasing the gas target pressure/length.

Waveform Reconstruction

Similarly to FROG and d-scan techniques, the pulse shape is not directly accessible from the measured spectrogram but has to be reconstructed using an iterative algorithm. The parameters that need to be retrieved from a measured TREX spectrogram are the following:

- the spectral phases of both pulses, including the CEPs
- the spectral intensities (based on an initial guess)
- the ratio between the pulse fluences
- the spectral transfer function of the optical setup

A retrieval algorithm needs to cope with a very large parameter space. It is also not possible to optimize each parameter independently; the algorithm thus needs to perform an optimization on the complete parameter space.

Thanks to their versatility and robustness, various flavors of evolutionary algorithms have become very popular in recent years for such black-box optimization problems [42]. Among many other things, they have been used for the retrieval of pulses from FROG [43] and d-scan measurements [44], for optimizing the driving pulses for coherent control experiments [45], and for retrieval of molecular information in high-harmonic spectroscopy [46]. These evolutionary algorithms can be seen as the precursors of the currently very active field of machine learning techniques developed for physical studies.

To reconstruct the waveforms from the measured spectrograms, we employ a custom evolutionary algorithm implemented in Julia [47]. Starting from a set of random initial guesses, called individuals, it optimizes the parameters of each individual by iteratively applying the following steps:

1. calculation of the fitness score for each individual
2. selection of the best individuals, called survivors, based on the fitness score
3. replacement of excluded individuals with new ones, obtained from the survivors via child generation rules
4. random mutation of a portion of individuals

During the optimization process, the resolution of the frequency axis, and correspondingly the length of the delay axis, is gradually increased from an initially low value (and short length) to the desired value, in order to decrease the retrieval time. Simultaneously, the population size is gradually decreased to reduce the computational cost. For more strongly chirped pulses, it has been proven beneficial to first perform a preoptimization step, where the spectral phase is described by a polynomial. Once a rough estimate of the spectral phase is obtained, it is used as the initial guess for the main retrieval. In this preoptimization step, the solver also optimizes the fluence ratio but does not yet change the spectral shape and transfer function. For the highest CEP and relative delay accuracy, a postoptimization step is implemented, where the solver exclusively optimizes those 2 parameters based on the result of the main retrieval. All 3 solver steps work on the same principle of evolutionary optimization described above. The implemented algorithm can retrieve a typical TREX measurement within 30 s to a few minutes on a standard personal computer, depending on the desired accuracy of the retrieval. More details on the retrieval algorithm implementation can be found in supplementary document Section S9.

Experimental setup

In our setup, the TO signal is generated in the same gas cell used to generate high-harmonics (1 mm long filled with helium at a backing pressure of 1 bar), thus allowing an in situ characterization of synthesized waveforms at the interaction position inside the vacuum chamber. The TO signal is then guided out of the chamber, spectrally filtered, and recorded. The vacuum chamber is needed only for the high-harmonic experiments and would not be necessary for the TREX measurements.

For the pulses used in this study, the TO signal extends down to 230 nm. UV-enhanced aluminum mirrors are necessary in order to preserve the short-wavelength part of the signal during

its propagation to the spectrometer. Since the copropagating fundamental spectra need to be attenuated before recording, it is necessary to use a filter with a cut-on wavelength of about 700 nm and a cut-off wavelength ideally below 230 nm. Typical color glass or thin-film filters do not allow such a broad transmission window while maintaining a sufficiently strong attenuation for the complete fundamental spectral region (700 to 2,200 nm). Therefore, we implemented the spatial filtering setup shown in Fig. 5. In this setup, the beam diameter is initially reduced through a telescope and then spatially dispersed with 2 UV-fused silica prisms. A sharp beam block is placed after the second prism in front of the back reflection mirror, providing a variable filter capable of completely removing the fundamentals. The reduced beam diameter allows for a sharper spectral cut. The filtered light is then spectrally recombined by back-propagating through the prism pair with a slight vertical tilt and focused into a commercial grating spectrometer (Ocean Optics USB2000+) via a CaF_2 lens.

This setup allows simple implementations of custom-shaped spectral filters that might be needed for different combinations of fundamental spectra. In our case, we record the spectra from a cut-on wavelength set around 650 nm down to 250 nm, limited by the reflectivity of the Al mirrors. An improved version of the spatial filtering setup was recently implemented utilizing only a single prism in a 4-f geometry (supplementary document Section S11).

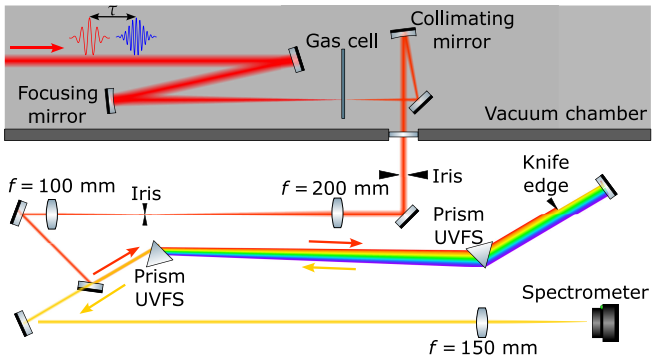

Fig. 5. Experimental setup used for the TREX measurements. Inside the vacuum chamber, the beam, consisting of 2 pulses, is focused into the gas cell where the TO signal is generated. After collimation, the beam exits the vacuum chamber and enters the spatial filtering setup used to remove the copropagating fundamentals. Here, after reducing the beam diameter with a telescope, the TO signal is spectrally dispersed by an ultraviolet (UV)-fused silica prism (UVFS). After collimation by a second prism, the fundamentals are removed with an adjustable knife edge. The signal propagates backward and is collected with a commercial spectrometer.

Results and Discussion

To showcase the full potential of the TREX technique, we characterized 2 CEP-stable few-cycle pulses, centered at 1,727 nm (IR pulse) and 804 nm (NIR pulse), respectively. Since these pulses are mutually coherent (stable φ_0 and φ_r), the total electric field, which we want to determine, has a duration of less than a single optical cycle if the pulses are close to temporal overlap. Initially, the pulse energies on target were about 200 μJ for the IR and 25 μJ for the NIR pulse. At these energies, we noticed the onset of the previously discussed high-intensity effects around time zero, which distorted the measured spectrogram. Therefore, the presented measurements were carried out after reducing the pulse energy by about a factor of 2. The measured spectrogram is shown in Fig. 6A. In order to avoid the

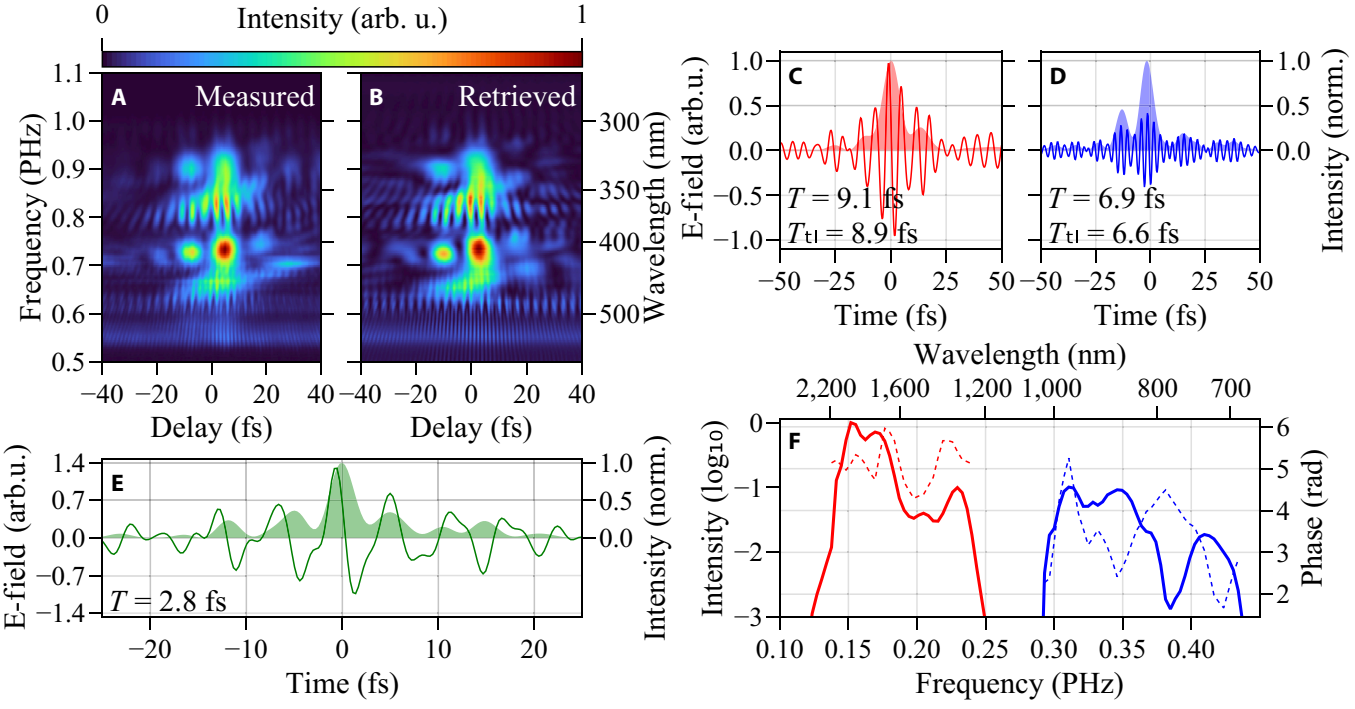

Fig. 6. Retrieval result of (A) a measured nonlinear spectrogram. (B) Retrieved spectrogram. (C and D) Reconstructed infrared (IR) and near-infrared (NIR) electric fields, intensity envelopes (shaded), and their intensity full width at half maximum pulse lengths T (and Fourier-limited T_{fl}). (E) Synthesized waveform for a relative delay of $\tau_0 = 1.35$ fs between the 2 constituent pulses. At a central wavelength of 1,560 nm, the pulse length of 2.8 fs corresponds to only 0.5 optical cycles. (F) Their spectral intensity (solid line) and retrieved spectral phases (dashed). The corresponding input spectra and transfer function are shown in supplementary document Section S10.

introduction of additional dispersion during attenuation, this is achieved through a set of interchangeable neutral density filters (ND 0.0 to ND 0.3). So as not to alter the dispersion, one of the filters is always present along the propagation path of the 2 pulses. The small thickness difference among the filter substrates, on the order of a few tens of microns, was precisely characterized via an interferometer.

During the TREX measurement, the delay between the 2 pulses was varied from −100 to 100 fs using the control system of the synthesizer [38]. This control system allows locking the CEP of both pulses and performing an interferometrically stable delay scan, meaning that random fluctuations of the delay are removed by the system. The high visibility of the fringe patterns, emerging from the interference of different nonlinear mixing signals, shows that interferometric stability is achieved during the scans. In particular, the φ_0-dependent fringes situated in the lower part of the spectrogram around 500 nm are clearly visible.

Similarly to FROG and d-scan, the quality of the pulse compression (of both pulses) can already be estimated reasonably well from the TREX spectrogram itself, even before running the retrieval algorithm. In general, the presence of dispersion leads to an asymmetric trace and, in particular, to tilted signals (e.g., second order) and/or signals present exclusively on one side of the trace (e.g., third order), as shown in Fig. 2 and Fig. S19. The fact that the highest-intensity peaks of the different mixing terms are reached at almost identical delays suggests that the pulses in this measurement are well compressed. This is confirmed by the retrieved pulse durations shown in Fig. 6C and D, which are very close to the Fourier limit. The appearance of a second bright spot next to the most intense central one suggests that 1 of the 2 pulses shows a noticeable pre- or postpulse. From the Fourier limit of the M-shaped spectrum, one would expect symmetric pre- and postpulses. The asymmetry in the brightness of the side signals thus indicates some remaining higher-order dispersion. This interpretation is confirmed by the retrieved NIR pulse, shown in Fig. 6D, that exhibits a noticeable prepulse. We also notice that the retrieved spectrogram shows a remarkable agreement with the measurement, indicating a successful convergence of the algorithm. As expected, the NIR pulse has substantially lower fluence than the IR pulse (see Fig. 6F), showing that the method can also be used to reconstruct pulses with different intensities accurately. Since this method enables us to characterize not only $E_1(t)$ and $E_2(t)$ but also the delay between them and the relative intensity, we can also accurately determine $E_{tot}(t)$, as shown in Fig. 6E. This results in a full width at half maximum pulse duration of 2.8 s, which corresponds to approximately half an optical cycle at a central wavelength of 1,560 nm. It is important to emphasize that the presented technique implicitly delivers the full set of synthesized waveforms that can be obtained by controlling the CEPs and relative delay between the pulses in a single measurement, since it retrieves both the individual constituent pulses as well as their relative arrival time difference with sub-cycle accuracy. This feature is of enormous use in multipulse waveform synthesizers as it greatly reduces the time spent characterizing the different synthesized waveforms. For this reason, we believe that the TREX technique represents a big step forward in the realization of waveform-controlled experiments [48].

In Fig. 7, we show simulated spectrograms corresponding to different pulse combinations that were inspired by experiments found in the literature [49,50]. The left panel shows

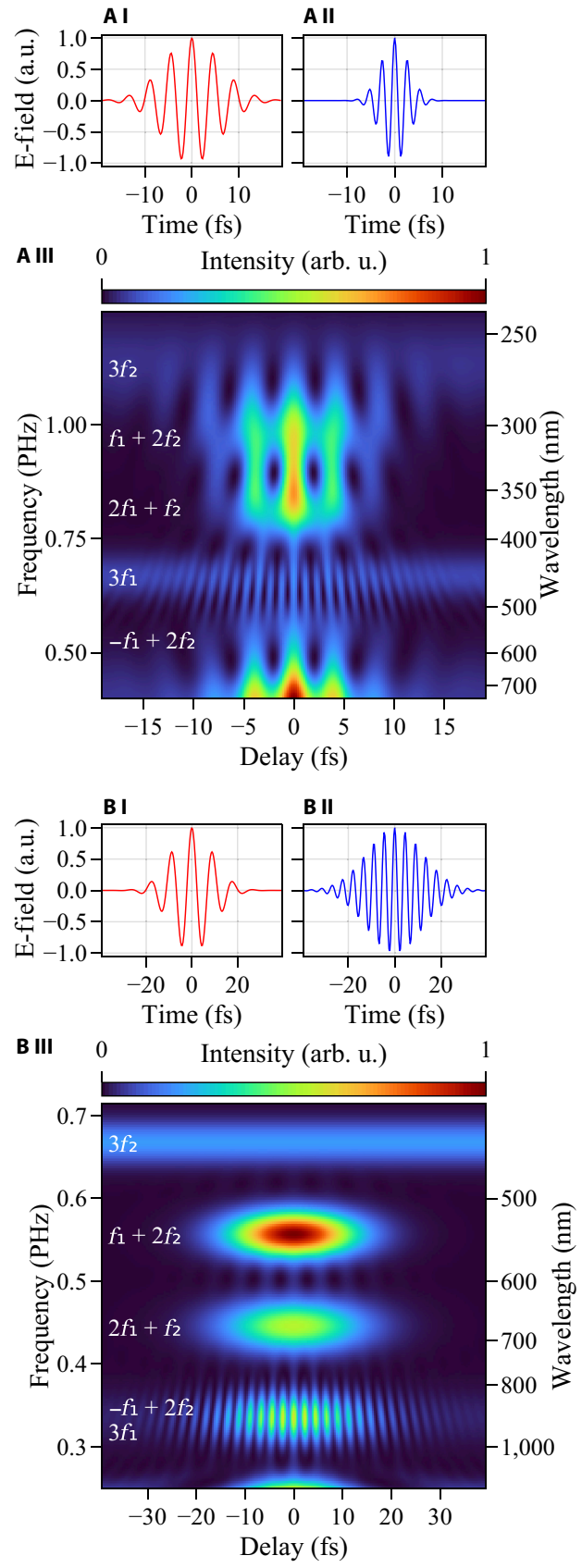

Fig. 7. Simulated TREX spectrograms for 2 different pulse combinations. (A) Few-cycle pulses around 1,350 and 800 nm (inspired by Barreau et al. [49]); (B) 15-fs-long mid-infrared (MIR) pulse at 2,700 nm and its second harmonic (inspired by Ritzkowsky et al. [50]).

the spectrogram obtained by interacting a few-cycle pulse from a Ti:sapphire-based system with a few-cycle pulse at 1,350 nm, which can be obtained via OPA. The right panel shows instead a mid-IR pulse at 2.7 μm interacting with a narrower second harmonic. Notice that in all these cases, φ_0-dependent signals are present in the spectrograms. Further simulations shown in supplementary document Section S8 suggest that the technique can as well be used when the durations of the 2 pulses differ significantly.

Conclusion

We have presented an all-optical measurement technique for the simultaneous complete electric field characterization of 2 synchronized pulses with different central wavelengths, including their CEPs. This technique can find application in various multicolor experiments, in particular those based on OPA sources. As shown, the TREX technique is applicable over a wide spectral region and with different pulse durations. Demonstrated here by exploiting the nonlinear response of a noble gas, this technique is likely applicable even in air at ambient pressure or using a glass plate with a few-micron thickness as a nonlinear medium.

The precise relative arrival time characterization offered by TREX, together with the complete knowledge of the interacting fields in situ, can be very useful for pump–probe spectroscopy as well as for strong-field experiments. The fast retrieval allows quick optimization of the compression and CEP at the interaction point, which is, for example, extremely important for attosecond pulse production via high-harmonic generation. Moreover, we believe that TREX represents a remarkable step toward waveform-controlled experiments, i.e., where different well-characterized optical waveforms are used to excite or probe a system. Detailed knowledge of the electric field is extremely important for modeling light–matter interaction, since fewer parameters need to be fitted in simulations. Furthermore, the exact determination of $E(t)$ allows precisely benchmarking the accuracy of the theoretical models involved.

Acknowledgments

M. Kubullek acknowledges support from the Max Planck School of Photonics and fruitful discussions with John P. Messerschmidt. The authors thank Phillip Junker for his support in implementing the new spatial filtering setup. F. Ritzkowsky acknowledges support from the Alexander von Humboldt Foundation.

Funding: This work was supported by the Helmholtz Association Program MML-Matter, by the Cluster of Excellence "CUI: Advanced Imaging of Matter" of the Deutsche Forschungsgemeinschaft (DFG) (EXC 2056 - project ID 390715994), and by PIER, the partnership of Universität Hamburg and DESY (grant ID PIF-2022-07).

Author contributions: M.K. and G.M.R. conceived the experimental technique. M.K., G.M.R., and R.E.M. built the experimental setup and implemented the data acquisition software. M.K., M.A.S.-T., R.E.M., F.S., and G.M.R. performed the experiments. M.K. developed the retrieval algorithm and simulation code with input from F.R., G.M.R., R.E.M., M.A.S.-T., and R.d.Q.G. All authors contributed to the interpretation of the simulation and experimental data. M.K. and G.M.R. wrote the manuscript with input from all authors. F.X.K. and G.M.R. supervised the project.

Competing interests: The authors declare that they have no competing interests.

Data Availability

The data that support the findings of this study are available from the authors upon request.

Supplementary Materials

Supplementary text
Figs. S1 to S22
Tables S1 to S5
Movie S1. Phi0Scan.mp4
Movie S2. PhiRScan.mp4

References

1. Geib NC, Zilk M, Pertsch T, Eilenberger F. Common pulse retrieval algorithm: A fast and universal method to retrieve ultrashort pulses. *Optica*. 2019;6(4):495–505.
2. Trebino R, Kane DJ. Using phase retrieval to measure the intensity and phase of ultrashort pulses: Frequency-resolved optical gating. *J Opt Soc Am A*. 1993;10(5):1101–1111.
3. Trebino R, DeLong KW, Fittinghoff DN, Sweetser JN, Krumbugel MA, Richman BA, Kane DJ. Measuring ultrashort laser pulses in the time frequency domain using frequency-resolved optical gating. *Rev Sci Instrum*. 1997;68(9): 3277–3295.
4. Miranda M, Fordell T, Arnold C, L'Huillier A, Crespo H. Simultaneous compression and characterization of ultrashort laser pulses using chirped mirrors and glass wedges. *Opt Express*. 2012;20:688–697.
5. Miranda M, Arnold CL, Fordell T, Silva F, Alonso B, Weigand R, L'Huillier A, Crespo H. Characterization of broadband few-cycle laser pulses with the d-scan technique. *Opt Express*. 2012;20(17):18732–18743.
6. Iaconis C, Walmsley I. Self-referencing spectral interferometry for measuring ultrashort optical pulses. *IEEE J Quantum Electron*. 1999;35(4):501–509.
7. Anderson ME, Monmayrant A, Gorza SP, Wasylczyk P, Walmsley IA. SPIDER: A decade of measuring ultrashort pulses. *Laser Phys Lett*. 2008;5(4):259–266.
8. Birge JR, Ell R, Kartner FX. Two-dimensional spectral shearing interferometry for few cycle pulse characterization. *Opt Lett*. 2006;31(13):2063–2065.
9. Borrego-Varillas R, Oriana A, Branchi F, Silvestri SD, Cerullo G, Manzoni C. Optimized ancillae generation for ultra-broadband two-dimensional spectral-shearing interferometry. *J Opt Soc Am B*. 2015;32(9):1851–1855.
10. Miranda M, Silva F, Neoricic L, Guo C, Pervak V, Canhota M, Silva AS, Sola IJ, Romero R, Guerreiro PT, et al. All-optical measurement of the complete waveform of octave-spanning ultrashort light pulses. *Opt Lett*. 2019;44(2):191–194.
11. Jones DJ, Diddams SA, Ranka JK, Windeler RS, Hall JL, Cundiff ST. Carrier-envelope phase control of femtosecond mode-locked lasers and direct optical frequency synthesis. *Science*. 2000;288(5466):635–639.
12. Sayler AM, Rathje T, Muller W, Ruhle K, Kienberger R, Paulus GG. Carrier-envelope phase measurement of ultrashort laser pulses. *Opt Lett*. 2011;36(1):1–3.

13. Herbst A, Scheffter K, Bidhendi MM, Kieker M, Srivastava A, Fattahi H. Recent advances in petahertz electric field sampling. *J Phys B Atomic Mol Phys*. 2022;55: Article 172001.
14. Kim KT, Zhang C, Shiner AD, Schmidt BE, Legare F, Villenueve DM, Corkum PB. Petahertz optical oscilloscope. *Nat Photonics*. 2013;7:958–962.
15. Park SB, Kim K, Cho W, Hwang SI, Ivanov I, Nam CH, Kim KT. Direct sampling of a light wave in air. *Optica*. 2018;5(4):402–408.
16. Korobenko A, Johnston K, Kubullek M, Arissian L, Dube Z, Wang T, Kübel M, Naumov AY, Villenueve DM, Kling MF, et al. Femtosecond streaking in ambient air. *Optica*. 2020;7(10):1372–1376.
17. Bionta MR, Ritzkowsky F, Turchetti M, Yang Y, Mor DC, Putnam WP, Kärtner FX, Berggren KK, Keathley PD. On-chip sampling of optical fields with attosecond resolution. *Nat Photonics*. 2021;15:456–460.
18. Wyatt AS, Witting T, Schiavi A, Fabris D, Matia-Hernando P, Walmsley IA, Marangos JP, Tisch JWG. Attosecond sampling of arbitrary optical waveforms. *Optica*. 2016;3(3): 303–310.
19. Goulielmakis E, Uiberacker M, Kienberger R, Baltuska A, Yakovlev V, Scrinzi A, Westerwalbesloh T, Kleineberg U, Heinzmann U, Drescher M, et al. Direct measurement of light waves. *Science*. 2004;305(5688):1267–1269.
20. Schiffrin A, Paasch-Colberg T, Karpowicz N, Apalkov V, Gerster D, Mühlbrandt S, Korbman M, Reichert J, Schultze M, Holzner S, et al. Optical-field-induced current in dielectrics. *Nature*. 2013;493(7430):70–74.
21. Sederberg S, Zimin D, Keiber S, Siegrist F, Wismer MS, Yakovlev VS, Floss I, Lemell C, Burgdörfer J, Schultze M, et al. Attosecond optoelectronic field measurement in solids. *Nat Commun*. 2020;11(1):Article 430.
22. Altwaijry N, Qasim M, Zimin D, Karpowicz N, Kling MF. Sensitivity enhancement in photoconductive light field sampling. *Adv Opt Mater*. 2024;12(12):Article 2302490.
23. Altwaijry N, Qasim M, Mamaikin M, Schötz J, Golyari K, Heynck M, Ridente E, Yakovlev VS, Karpowicz N, Kling MF. Broadband photoconductive sampling in gallium phosphide. *Adv Opt Mater*. 2023;11(9):Article 2202994.
24. Ridente E, Mamaikin M, Altwaijry N, Zimin D, Kling MF, Pervak V, Weidman M, Krausz F, Karpowicz N. Electro-optic characterization of synthesized infrared-visible light fields. *Nat Commun*. 2022;13(1):Article 1111.
25. Crespo HM, Witting T, Canhota M, Miranda M, Tisch JWG. *In situ* temporal measurement of ultrashort laser pulses at full power during high-intensity laser–matter interactions. *Optica*. 2020;7(8):995–1002.
26. Awad M, Manna A, Hell S, Ying B, Ábrók L, Divéki Z, Cormier E, Kiss B, Böhmer J, Böhmer J, et al. Few-cycle laser pulse characterization on-target using high-harmonic generation from nano-scale solids. *Opt Express*. 2024;32(2):1325–1333.
27. Maiuri M, Garavelli M, Cerullo G. Ultrafast spectroscopy: State of the art and open challenges. *J Am Chem Soc*. 2020;142(1):3–15.
28. Oishi Y, Kaku M, Suda A, Kannari F, Midorikawa K. Generation of extreme ultraviolet continuum radiation driven by a sub-10-fs two-color field. *Opt Express*. 2006;14(16): 7230–7237.
29. Koulouklidis AD, Gollner C, Shumakova V, Fedorov VY, Pugžlys A, Baltuška A, Tzortzakis S. Observation of extremely efficient terahertz generation from mid-infrared two-color laser filaments. *Nat Commun*. 2020;11(1):Article 292.
30. Wanie V, Bloch E, Månsson EP, Colaizzi L, Ryabchuk S, Saraswathula K, Ordonez AF, Ayuso D, Smirnova O, Trabattoni A, et al. Capturing electron-driven chiral dynamics in UV excited molecules. *Nature*. 2024;630(8015):109–115.
31. Jiang Y, Messerschmidt JP, Scheiba F, Tyulnev I, Wang L, Wei Z, Rossi GM. Ultraviolet pulse compression via cross-phase modulation in a hollow-core fiber. *Optica*. 2024;11(2):291–296.
32. Seifert B, Stolz H. A method for unique phase retrieval of ultrafast optical fields. *Meas Sci Technol*. 2008;20(1): Article 015303.
33. Wong TC, Ratner J, Chauhan V, Cohen J, Vaughan PM, Xu L, Consoli A, Trebino R. Simultaneously measuring two ultrashort laser pulses on a single-shot using double-blind frequency-resolved optical gating. *J Opt Soc Am A*. 2012;29(6):1237–1244.
34. Stibenz G, Steinmeyer G. Interferometric frequency-resolved optical gating. *Opt Express*. 2005;13(7):2617–2626.
35. Rossi GM, Mainz RE, Yang Y, Scheiba F, Silva-Toledo MA, Chia S-H, Keathley PD, Fang S, Mücke OD, Manzoni C, et al. Sub-cycle millijoule-level parametric waveform synthesizer for attosecond science. *Nat Photonics*. 2020;14:629–635.
36. Brahms C, Travers JC. Luna.Jl. Zenodo. 9 Dec 2023. http://doi.org/10.5281/zenodo.10323704
37. Malitson IH. Interspecimen comparison of the refractive index of fused silica. *J Opt Soc Am*. 1965;55(10):1205–1209.
38. Mainz RE, Rossi GM, Scheiba F, Silva-Toledo MA, Yang Y, Cirmi G, Kärtner FX. Parametric waveform synthesis: A scalable approach to generate sub-cycle optical transients. *Opt Express*. 2023;31(7):11363–11394.
39. Ivanov MY, Spanner M, Smirnova O. Anatomy of strong field ionization. *J Mod Opt*. 2005;52(2–3):165–184.
40. Blanc SPL, Sauerbrey R, Rae SC, Burnett K. Spectral blue shifting of a femtosecond laser pulse propagating through a high-pressure gas. *J Opt Soc Am B*. 1993;10(10):1801–1809.
41. Brunel F. Harmonic generation due to plasma effects in a gas undergoing multiphoton ionization in the high-intensity limit. *J Opt Soc Am B*. 1990;7(4):521–526.
42. Vikhar PA. Evolutionary algorithms: A critical review and its future prospects. In: *2016 international conference on global trends in signal processing, information computing and xommunication (ICGTSPICC)* New York (NY): IEEE; 2016. p. 261–265.
43. Hyyti J, Escoto E, Steinmeyer G. Pulse retrieval algorithm for interferometric frequency resolved optical gating based on differential evolution. *Rev Sci Instrum*. 2017;88(10): Article 103102.
44. Escoto E, Tajalli A, Nagy T, Steinmeyer G. Advanced phase retrieval for dispersion scan: A comparative study. *J Opt Soc Am B*. 2017;35(1):8–19.
45. Zeidler D, Frey S, Kompa KL, Motzkus M. Evolutionary algorithms and their application to optimal control studies. *Phys Rev A*. 2001;64:Article 023420.
46. Jiang C, Jiang H, Chen Y, Li B, Lin CD, Jin C. Genetic-algorithm retrieval of the molecular alignment distribution with high-order harmonics generated from transiently aligned CO_2 molecules. *Phys Rev A*. 2022;105:Article 023111.
47. Bezanson J, Edelman A, Karpinski S, Shah VB. Julia: A fresh approach to numerical computing. *SIAM Rev*. 2017;59(1):65–98.

48. Cirmi G, Mainz RE, Silva-Toledo MA, Scheiba F, Çankaya H, Kubullek M, Rossi GM, Kärtner FX. Optical waveform synthesis and its applications. *Laser Photonics Rev*. 2023;17(4):Article 2200588.
49. Barreau L, Ross AD, Garg S, Kraus PM, Neumark DM, Leone SR. Efficient table-top dual-wavelength beamline for ultrafast transient absorption spectroscopy in the soft X-ray region. *Sci Rep*. 2020;10(1):Article 5773.
50. Ritzkowsky F, Bebeti E, Rossi GM, Mainz RE, Suchowski H, Cankaya H, Kärtner FX. Passively CEP stable Sub-2-cycle source in the mid-infrared by adiabatic difference frequency generation. *Opt Lett*. 2023;48(7):1870–1873.